

# ANALYSIS OF THE NUMERICAL DISPERSION OF WAVES IN SATURATED POROELASTIC MEDIA

Fabio I. Zyserman<sup>a</sup> and Juan E. Santos<sup>a,b</sup>

<sup>a</sup>*CONICET, Fac. de Cs. Astronómicas y Geofísicas, UNLP, Paseo del Bosque s/n, 1900 - La Plata, Argentina; zyserman@fcaglp.unlp.edu.ar*

<sup>b</sup>*Department of Mathematics, Purdue University, 150 N. University Street, West Lafayette, Indiana, 47907-2067, USA; santos@math.purdue.edu*

**Abstract.** This work presents the analysis of the numerical dispersion properties of a finite element method used to approximate the solution of the equations of motion for a fluid saturated porous elastic solid (a Biot medium) in the two dimensional case and the low frequency regime. The finite element method employed comprises a nonconforming rectangular element for the approximation of each component of the displacement vector in the solid phase, and the Raviart-Thomas-Nedelec mixed finite element space of zero order for the fluid phase.

The study is performed by constructing and analyzing analytic and numerical dimensionless dispersion relations, and by evaluating derived quantities such as dimensionless phase and group velocities and dimensionless attenuation for the three type of waves predicted by Biot's equations of motion as a measure of the numerical distortion. It is observed that the finite element procedure introduces both numerical dispersion and anisotropy, being the slow wave the most affected by this effects. The analysis presented yields lower bounds for the number of points per wavelength needed to reach a desired accuracy in the dimensionless phase and group velocities and attenuation coefficients in Biot media.

**Keywords:**

Numerical dispersion, Poroelasticity, Finite element methods

PACS: 65P25, 77A99, MSC: 65N99

**1 INTRODUCTION**

The propagation of waves in a porous elastic solid saturated by a single-phase compressible viscous fluid was first analyzed by Biot in several classic papers (1; 2; 3). In Biot's theory the two-phase material is considered as a continuum and the macroscopic variables follow the laws of continuum mechanics. The theory assumes that anelastic effects arise from viscous interaction between the solid and the fluid. Biot predicted the existence of two compressional waves: the type I or fast wave for which the solid and fluid displacements are in phase, and the type II or slow wave for which the displacements are out of phase. The type I and shear waves have a behavior similar to those in an elastic solid, with high phase velocities, low attenuation and very little dispersion. At low frequencies, the slow wave is diffusive, since viscosity effects dominate (the boundary layer is thick compared to the pore size). At high frequencies, tangential slip occurs (the boundary layer is thin), inertial effects dominate and the slow wave becomes a propagation mode. This wave contributes to the attenuation of the fast waves by mode conversions at heterogeneities. For shortness, a porous elastic solid saturated by a single-phase fluid will be referred to as a Biot medium.

The purpose of this paper is to analyze the numerical dispersion associated with the numerical solution of Biot's equations of motion in the 2D case employing the finite element method presented in (4), where optimal *a priori* error estimates are derived. The procedure employs the nonconforming rectangular element defined in (5) to approximate each component of the displacement vector in the solid phase. On the other hand, the displacement in the fluid phase is approximated using the vector part of the Raviart-Thomas-Nedelec mixed finite element space of zero order ( $RTN_0$ ), which is a conforming space (6; 7).

The knowledge of the dispersive properties of any numerical procedure is of practical importance, since an underestimation of their relevance can lead to significant numerical error. This is of particular importance for the case of numerical simulation based on Biot's equations of motion; from which it is desirable to obtain synthetic seismograms where physical attenuation and dispersion effects be accurately modeled. In spite of the fact that Biot's equations of motion have been widely used to simulate wave propagation in fluid saturated poroelastic materials using a variety of numerical procedures, to the authors' knowledge this is the first time that a numerical dispersion analysis for these equations is performed.

This work is based on some previous results on the subject. The dispersive effects in the numerical solution of the scalar wave equation has been investigated in References (8; 9; 10; 11; 12), while the elastic case was analyzed in References (13; 14; 15; 16). For the former, a wide variety of numerical dispersion reducing methods (17; 18; 19; 20; 21; 22; 23; 24; 25) have been developed.

The choice of the nonconforming rectangular element defined in (5) to approximate the solid displacement vector is based on the dispersion analysis presented in (15), where it is shown that employing this nonconforming element allows to approximately halve the number of points per wavelength necessary to reach a desired tolerance in the numerical dispersion, as compared with the standard  $Q_1$  conforming elements.

The organization of the paper is as follows. In Section 2 a review of Biot's theory of wave propagation in fluid saturated poroelastic media is presented, including the calculation of phase

velocities and attenuation coefficients for each type of wave. Section 3 presents the boundary value problem to be analyzed, together with an associated weak formulation. In Section 4 the finite element spaces and the global finite element procedure to be analyzed are presented. Also, a result derived in (4) concerning *a-priori* error estimates for the algorithm is stated. Section 5 is devoted to the numerical dispersion analysis of the finite element procedure, and Section 6 illustrates the application of the analysis when the Biot medium is a sample of gas saturated Berea sandstone. Finally, the conclusions are drawn in Section 7.

## 2 REVIEW OF BIOT'S THEORY

Consider a porous solid saturated by a single phase, compressible viscous fluid and assume that the whole aggregate is isotropic. Let  $u^s = (u_i^s(x, \omega))$  and  $\tilde{u}^f = (\tilde{u}_i^f(x, \omega))$ ,  $i = 1, 2$  denote the averaged displacement vectors of the solid and fluid phases at the angular frequency  $\omega$  respectively. Also let

$$u^f = u^f(x, \omega) = \phi(\tilde{u}^f - u^s),$$

be the average relative fluid displacement per unit volume of bulk material, where  $\phi$  denotes the effective porosity. Also set  $u = (u^s, u^f)$  and note that

$$\xi = -\nabla \cdot u^f,$$

represents the change in fluid content.

Let  $\tau_{ij}$ ,  $i, j = 1, 2$ , and  $p_f$  denote the the stress tensor of the bulk material and the fluid pressure, respectively. Following (3), the stress-strain relations, stated in the space-frequency domain, can be written in the form:

$$\begin{aligned} \tau_{ij}(u) &= 2\mu \varepsilon_{ij}(u^s) + \delta_{ij}(\lambda_c \nabla \cdot u^s - D \xi), \\ p_f(u) &= -D \nabla \cdot u^s + K_{av} \xi, \end{aligned} \quad (1)$$

where  $\varepsilon_{ij}(u^s)$  denotes the strain tensor of the solid. The coefficient  $\mu$  is equal to the shear modulus of the bulk material, considered to be equal to the shear modulus of the dry matrix. Also

$$\lambda_c = K_c - \mu,$$

with  $K_c$  being the bulk modulus of the saturated material. Following (26; 27) the coefficients  $K_c$ ,  $D$  and  $K_{av}$  in (1) can be obtained from the relations

$$\begin{aligned} \alpha &= 1 - \frac{K_m}{K_s}, \quad K_{av} = \left[ \frac{\alpha - \phi}{K_s} + \frac{\phi}{K_f} \right]^{-1} \\ K_c &= K_m + \alpha^2 K_{av}, \quad D = \alpha K_{av}, \end{aligned} \quad (2)$$

where  $K_s$ ,  $K_m$  and  $K_f$  denote the bulk modulus of the solid grains composing the solid matrix, the dry matrix and the the saturant fluid, respectively. The coefficient  $\alpha$  is known as the effective stress coefficient of the bulk material.

### 2.1 The equations of motion

Let  $\rho_s$  and  $\rho_f$  denote the mass densities of the solid grains and of the fluid, respectively and let

$$\rho = (1 - \phi)\rho_s + \phi\rho_f \quad (3)$$

denote the mass density of the bulk material. Define the positive definite matrix  $\mathcal{P}$  and the nonnegative matrix  $\mathcal{B}$  by

$$\mathcal{P} = \begin{pmatrix} \rho I & \rho_f I \\ \rho_f I & g I \end{pmatrix}, \quad \mathcal{B} = \begin{pmatrix} 0I & 0I \\ 0I & bI \end{pmatrix},$$

where  $I$  denotes the identity matrix in  $R^{2 \times 2}$ . The mass coupling coefficient  $g$  represents the inertial effects associated with dynamic interactions between the solid and fluid phases, while the coefficient  $b$  includes the viscous coupling effects between such phases. They are given by the relations

$$b = \frac{\eta}{k}, \quad g = \frac{S\rho_f}{\phi}, \quad S = \frac{1}{2} \left( 1 + \frac{1}{\phi} \right), \quad (4)$$

where  $\eta$  is the fluid viscosity and  $k$  the absolute permeability.  $S$  is known as the structure or tortuosity factor. Above a certain critical frequency  $\omega_t$  the coefficients  $b$  and  $g$  become frequency dependent (2; 28; 29). This effect is associated with the departure of the flow from the laminar Poiseuille type at the pore scale, which occurs for frequencies greater than  $\omega_t$ . The value of  $\omega_t$  can be estimated by the formula (30)

$$\omega_t = \frac{2\eta\phi}{\rho_f(a_p)^2}, \quad (5)$$

where  $a_p$  is the effective flow channel or pore size parameter. Following the ideas in (31; 32), it can be expressed in the form

$$a_p = 2 \left( \frac{A_0 k}{\phi} \right)^{1/2}, \quad (6)$$

where  $A_0$  denotes the Kozeny-Carman constant (33).

In this article the analysis is restricted to the low-frequency case. The ideas presented here can be used to treat the high-frequency case that will be the subject of a forthcoming publication.

Next, let  $\mathcal{L}(u)$  be the second order differential operator defined by

$$\mathcal{L}(u) = (\nabla \cdot \sigma(u), -\nabla p_f(u))^t.$$

Then if  $\omega = 2\pi f$  is the angular frequency and  $\mathcal{F}(x, \omega) = (\mathcal{F}^s(x, \omega), \mathcal{F}^f(x, \omega))$  is the external source, the equations of motion, stated in the space-frequency domain, are (1; 2)

$$-\omega^2 \mathcal{P}u(x, \omega) + i\omega \mathcal{B}u(x, \omega) - \mathcal{L}(u(x, \omega)) = \mathcal{F}(x, \omega). \quad (7)$$

## 2.2 Phase velocities and attenuation

Set the source term  $\mathcal{F}$  to zero in (7) and consider first a standing compressional plane wave in the plane  $(x_1, x_2)$ , and define the potentials

$$\varphi = A_c e^{-iq \cdot x} \quad \psi = B_c e^{-iq \cdot x}$$

where

$$q = (q_1, q_2) = (q_1^{(r)} - i q_1^{(i)}, q_2^{(r)} - i q_2^{(i)}) \equiv q^{(r)} - i q^{(i)}, \quad (8)$$

and  $q \cdot x = q_1 x_1 + q_2 x_2$ . Introducing  $u^s = \nabla \varphi$  and  $u^f = \nabla \psi$  in (7) the following equations are obtained:

$$\begin{aligned} (\rho\omega^2 - H_c q^2)A_c + (\rho_f \omega^2 - Dq^2)B_c &= 0, \\ (\rho_f \omega^2 - Dq^2)A_c + (g\omega^2 - i\omega b - Mq^2)B_c &= 0, \end{aligned} \quad (9)$$

where  $q^2 = q \cdot q$ .

The fact that the strain and kinetic energies are positive allows one to choose two physically meaningful roots  $q_1$  and  $q_2$  of  $q$  in (9) having negative imaginary part, corresponding to the type I and type II compressional waves, respectively.

In a similar fashion, for the shear waves consider potentials

$$\varphi = A_S e^{-iq \cdot x}, \quad \psi = B_S e^{-iq \cdot x}.$$

Introducing the corresponding displacements  $u^s = \left( -\frac{\partial \varphi}{\partial x_2}, \frac{\partial \varphi}{\partial x_1} \right)$  and  $u^f = \left( -\frac{\partial \psi}{\partial x_2}, \frac{\partial \psi}{\partial x_1} \right)$  in (7) yields the equation

$$q_S^2 = \frac{\omega^2}{\mu} \left( \rho - \frac{\rho_f^2}{g - ib/\omega} \right). \quad (10)$$

In the above equation the root  $q_S$  with negative imaginary part is chosen, as was done for the compressional waves.

Notice that equations (9) and (10) involve angles  $\theta_{2,j}$  between vectors  $q_j^{(r)}$  and  $q_j^{(i)}$ ,  $j = I, II, S$  respectively, which depend only on the physical parameters of the model, that have to be calculated in order to completely determine the dispersion relations. The phase velocities  $c_j$  and attenuation  $\xi_j$  (measured in  $dB$ ) for each one of the waves are usually given by the formulas (26)

$$c_j = \omega / |q_j^{(r)}| \quad (11)$$

$$a_j = 2\pi \cdot 8.685889 |q_j^{(i)}| / |q_j^{(r)}|, \quad j = I, II, S, \quad (12)$$

For the attenuation,  $\xi_j = |q_j^{(i)}|$ ,  $j = I, II, S$  is also used. The second choice is the one employed in this paper.

### 3 THE DIFFERENTIAL PROBLEMS AND A VARIATIONAL FORMULATION

Consider the solution of Biot equations of motion (7) in a rectangular domain  $\Omega$  with boundary  $\Gamma$ . In order to completely define a boundary value problem, a boundary condition must be given. Let therefore  $\nu$  and  $\chi$  denote the unit outer normal and a unit tangent on  $\Gamma$ , respectively, so that  $\{\nu, \chi\}$  is an orthonormal system on  $\Gamma$ . Then, set

$$\mathcal{G}_\Gamma(u) = \left( \tau(u)\nu \cdot \nu, \tau(u)\nu \cdot \chi, p_f(u) \right)^t, \quad (13a)$$

$$S_\Gamma(u) = (u^s \cdot \nu, u^s \cdot \chi, u^f \cdot \nu)^t. \quad (13b)$$

The following absorbing boundary condition, which was derived in (34), will be used:

$$-\mathcal{G}_\Gamma(u(x, \omega)) = i\omega \mathcal{D} S_\Gamma(u(x, \omega)), \quad (x, \omega) \in \Gamma \times (0, \omega^*), \quad (14)$$

where  $\omega^*$  is an upper bound for the frequencies of interest. The matrix  $\mathcal{D}$  in Eq. (14) is positive definite, and is given by the following relations:  $\mathcal{D} = \mathcal{A}^{\frac{1}{2}} \mathcal{N}^{\frac{1}{2}} \mathcal{A}^{\frac{1}{2}}$ , where  $\mathcal{N} = \mathcal{A}^{-\frac{1}{2}} \mathcal{M}^{\frac{1}{2}} \mathcal{A}^{-\frac{1}{2}}$  and

$$\mathcal{A} = \begin{pmatrix} \rho & 0 & \rho_f \\ 0 & \rho - \frac{(\rho_f)^2}{g} & 0 \\ \rho_f & 0 & g \end{pmatrix}, \quad \mathcal{M} = \begin{pmatrix} \lambda_c + 2\mu & 0 & \alpha K_{av} \\ 0 & \mu & 0 \\ \alpha K_{av} & 0 & K_{av} \end{pmatrix}. \quad (15)$$

In order to state a variational formulation for (7) with the boundary condition (14) some notation must be introduced. For  $X \subset \mathbb{R}^2$  with boundary  $\partial X$ , let  $(\cdot, \cdot)_X$  and  $\langle \cdot, \cdot \rangle_{\partial X}$  denote the complex  $L^2(X)$  and  $L^2(\partial X)$  inner products for scalar, vector, or matrix valued functions. Also, for  $s \in \mathbb{R}$ ,  $\|\cdot\|_{s,X}$  and  $|\cdot|_{s,X}$  will denote the usual norm and seminorm for the Sobolev space  $H^s(X)$ . In addition, if  $X = \Omega$  or  $X = \Gamma$ , the subscript  $X$  may be omitted such that  $(\cdot, \cdot) = (\cdot, \cdot)_{\Omega}$  or  $\langle \cdot, \cdot \rangle = \langle \cdot, \cdot \rangle_{\Gamma}$ . Also, set

$$\begin{aligned} H(\operatorname{div}; \Omega) &= \{v \in [L^2(\Omega)]^2 : \nabla \cdot v \in L^2(\Omega)\}, \\ H^1(\operatorname{div}; \Omega) &= \{v \in [H^1(\Omega)]^2 : \nabla \cdot v \in H^1(\Omega)\}, \end{aligned}$$

with the norms

$$\|v\|_{H(\operatorname{div}; \Omega)} = [\|v\|_0^2 + \|\nabla \cdot v\|_0^2]^{1/2}; \quad \|v\|_{H^1(\operatorname{div}; \Omega)} = [\|v\|_1^2 + \|\nabla \cdot v\|_1^2]^{1/2}.$$

Considering the space  $\mathcal{V} = [H^1(\Omega)]^2 \times H(\operatorname{div}; \Omega)$ , multiply equation (7) by  $v \in \mathcal{V}$ , use integration by parts and apply the boundary condition (14) to see that the solution  $u$  of (7) and (14) satisfies *the weak form*:

$$\begin{aligned} -\omega^2 (\mathcal{P}u, v) + i\omega (\mathcal{B}u, v) + \mathcal{A}(u, v) + i\omega \langle \mathcal{D} S_{\Gamma}(u), S_{\Gamma}(v) \rangle &= (\mathcal{F}, v), \\ v = (v^{(1)}, v^{(2)})^t \in \mathcal{V}, \end{aligned} \quad (16)$$

where  $\mathcal{A}(u, v)$  is the bilinear form defined as follows:

$$\mathcal{A}(u, v) = (\tau_{jk}(u), \varepsilon_{jk}(v^{(1)})) - (p_f(u), \nabla \cdot v^{(2)}), \quad u, v \in \mathcal{V}. \quad (17)$$

In (17) Einstein's convention of sum on repeated indices is used.

#### 4 THE FINITE ELEMENT PROCEDURE

The numerical procedures to approximate the solution of (16) will be defined and analyzed for the case of rectangular elements. Let  $\mathcal{T}^h(\Omega)$  be a nonoverlapping partition of  $\Omega$  into rectangles  $\Omega_j$  of diameter bounded by  $h$  such that  $\overline{\Omega} = \cup_{j=1}^J \overline{\Omega}_j$ . Denote by  $m_j$  and  $m_{jk}$  the midpoints of  $\partial\Omega_j \cap \Gamma$  and  $\partial\Omega_j \cap \partial\Omega_k$ , respectively.

To approximate each component of the solid displacement vector the 2D nonconforming finite element space  $\mathcal{N}C^h$  defined in (5) is employed, while to approximate the fluid displacement vector the vector part of the Raviart-Thomas-Nedelec space (6; 7) of zero order, denoted  $\mathcal{W}^h$  is chosen. More specifically, set

$$\widehat{R} = [-1, 1]^2, \quad \widehat{\mathcal{N}C}(\widehat{R}) = \operatorname{Span}\{1, \widehat{x}_1, \widehat{x}_2, \alpha(\widehat{x}_1) - \alpha(\widehat{x}_2)\}, \quad \alpha(\widehat{x}_1) = \widehat{x}_1^2 - \frac{5}{3}\widehat{x}_1^4,$$

with the degrees of freedom being the values at the midpoint of each edge of  $\widehat{R}$ .

Also, if  $\psi^L(\widehat{x}_1) = \frac{-1+\widehat{x}_1}{2}$ ,  $\psi^R(\widehat{x}_1) = \frac{1+\widehat{x}_1}{2}$ ,  $\psi^B(\widehat{x}_2) = \frac{-1+\widehat{x}_2}{2}$ ,  $\psi^T(\widehat{x}_2) = \frac{1+\widehat{x}_2}{2}$ , set

$$\widehat{\mathcal{W}}(\widehat{R}) = \text{Span}\{(\psi^L(\widehat{x}_1), 0)^t, (\psi^R(\widehat{x}_1), 0)^t, (0, \psi^B(\widehat{x}_2))^t, (0, \psi^T(\widehat{x}_2))^t\}.$$

Next, for each  $\Omega_j$ , let  $F_{\Omega_j} : \widehat{R} \rightarrow \Omega_j$  be an invertible affine mapping such that  $F_{\Omega_j}(\widehat{R}) = \Omega_j$ , and define

$$\begin{aligned} \mathcal{NC}_j^h &= \{v = (v_1, v_2)^t : v_i = \widehat{v}_i \circ F_{\Omega_j}^{-1}, \widehat{v}_i \in \widehat{\mathcal{NC}}(\widehat{R}), i = 1, 2\}, \\ \mathcal{W}_j^h &= \{w : w = \widehat{w} \circ F_{\Omega_j}^{-1}, \widehat{w} \in \widehat{\mathcal{W}}(\widehat{R})\}. \end{aligned}$$

Then the finite element spaces  $\mathcal{NC}^h$  and  $\mathcal{W}^h$  are defined as follows:

$$\begin{aligned} \mathcal{NC}^h &= \{v : v_j = v|_{\Omega_j} \in \mathcal{NC}_j^h, v_j(m_{jk}) = v_k(m_{jk}) \forall (j, k)\}, \\ \mathcal{W}^h &= \{w \in H(\text{div}; \Omega) : w_j = w|_{\Omega_j} \in \mathcal{W}_j^h\}. \end{aligned}$$

Note that standard approximation theory implies that, for all  $\varphi = (\varphi^{(1)}, \varphi^{(2)})^t \in [H^2(\Omega)]^2 \times H^1(\text{div}; \Omega)$ ,

$$\inf_{p \in \mathcal{NC}^h} \left[ \|\varphi^{(1)} - p\|_0 + h \left( \sum_j \|\varphi^{(1)} - p\|_{1, \Omega_j}^2 \right)^{\frac{1}{2}} \right] \leq Ch^2 \|\varphi^{(1)}\|_2, \quad (18a)$$

$$\inf_{p \in \mathcal{W}^h} \|\varphi^{(2)} - p\|_0 \leq Ch \|\varphi^{(2)}\|_1, \quad (18b)$$

$$\inf_{p \in \mathcal{W}^h} \|\varphi^{(2)} - p\|_{H(\text{div}; \Omega)} \leq Ch (\|\varphi^{(2)}\|_1 + \|\nabla \cdot \varphi^{(2)}\|_1). \quad (18c)$$

Next, the global finite element space to approximate the solution  $u$  of (16) is defined by

$$\mathcal{V}^h = \mathcal{NC}^h \times \mathcal{W}^h. \quad (19)$$

Set

$$\mathcal{A}_h(u, v) = \sum_j \left[ (\tau_{jk}(u), \varepsilon_{jk}(v^{(1)}))_{\Omega_j} - (p_f(u), \nabla \cdot v^{(2)})_{\Omega_j} \right] \quad (20)$$

and

$$\Theta_h(u, v) = -\omega^2 (\mathcal{P}u, v) + i\omega (\mathcal{B}u, v) + \mathcal{A}_h(u, v) + i\omega \langle \mathcal{D} S_\Gamma(u), S_\Gamma(v) \rangle. \quad (21)$$

Finally the global finite element procedure is defined as follows: find  $u^h = (u^{(s,h)}, u^{(f,h)})^t \in \mathcal{V}^h$  such that

$$\Theta_h(u^h, v) = (\mathcal{F}, v), \quad v = (v^{(1)}, v^{(2)})^t \in \mathcal{V}^h. \quad (22)$$

The arguments given in (4) shows that problem (22) has a unique solution for any  $\omega \neq 0$  and that the following apriori error estimates hold: Let  $u \in \mathcal{V}$  and  $u^h \in \mathcal{V}^h$  be the solutions of (16) and (22), respectively. Then, the following is the energy-norm error estimate: for sufficiently small  $h > 0$ ,

$$\|u^s - u^{(s,h)}\|_{1,h} + \|\nabla \cdot (u^f - u^{(f,h)})\|_0 \leq C(\omega)h \left[ \|u^s\|_2 + \|u^f\|_{\frac{3}{2}} + \|\nabla \cdot u^f\|_1 \right].$$

Also, the  $[L^2(\Omega)]^4$ -error estimate is as follows: for sufficiently small  $h > 0$ ,

$$\|u - u^h\|_0 \leq C(\omega) \left[ h^2 \left( \|u^s\|_2 + \|u^f\|_{\frac{3}{2}} \right) + h (\|u^f\|_1 + \|\nabla \cdot u^f\|_1) \right].$$

## 5 NUMERICAL DISPERSION ANALYSIS

The solutions to equations (9) and equation (10) are written, as a first step, in dimensionless form. For that purpose define the following dimensionless parameters for the case of non-zero viscosity:

$$\delta_1 = \frac{\mu}{\lambda_c + 2\mu}, \quad \delta_2 = \frac{D}{\lambda_c + 2\mu}, \quad \delta_3 = \frac{M}{\lambda_c + 2\mu}, \quad (23)$$

$$(24)$$

$$\omega_c = \frac{b}{\phi\rho_f}, \quad \omega_a = \frac{\omega}{\omega_c}, \quad (25)$$

$$\gamma_1 = \frac{\rho_f}{\rho}, \quad \gamma_2 = \frac{g}{\rho}, \quad \gamma_3 = \frac{b}{\rho\omega_c}. \quad (26)$$

and a reference velocity  $V_R = \sqrt{\frac{\lambda_c + 2\mu}{\rho}}$ . The solutions to equations (9) for the non-zero viscosity case can now be written in dimensionless form yielding the following dispersion relation

$$\frac{1}{(\tilde{c})^2} = \frac{V_R^2}{\omega^2} q^2 = \left( \frac{1}{2(-\delta_2^2 + \delta_3)} \left( (\gamma_2 + i\frac{\gamma_3}{\omega_a} - 2\gamma_1\delta_2 + \delta_3) \mp \sqrt{\left( \gamma_2 + i\frac{\gamma_3}{\omega_a} - 2\gamma_1\delta_2 + \delta_3 \right)^2 - 4 \left( -\gamma_1^2 + \gamma_2 + i\frac{\gamma_3}{\omega_a} \right) (-\delta_2^2 + \delta_3)} \right) \right), \quad (27)$$

where the  $\mp$  signs stands for the fast and slow compressional waves respectively. The corresponding dispersion relation for the shear wave is

$$\frac{1}{(\tilde{c})^2} = \frac{V_R^2}{\omega^2} q^2 = \left( \frac{-\gamma_1^2 + \gamma_2 + i\frac{\gamma_3}{\omega_a}}{(\gamma_2 + i\frac{\gamma_3}{\omega_a})\delta_1} \right). \quad (28)$$

In the zero-viscosity case, the dispersion relations (27) and (28) are still valid setting to zero all the imaginary terms.

In order to proceed, set the source term to zero in Eq. (22) and consider only a portion of the domain far away from the artificial boundaries so that their contribution can be neglected (35). Further, assume that the grid is homogeneous and the elements  $\Omega_j$  are square with side length  $h$ .

To perform the discrete dispersion analysis, a stencil without a preferred direction must be defined (36; 23; 16). If the stencil in Fig.(1a) composed of two nonconforming elements - comprising seven nodes-, is considered, it turns out that this stencil has a preferred orientation, and therefore does not appropriately represent the whole mesh. Then the four two-domains stencils as in Fig. (1b) are combined in order to get the smallest stencil  $\tilde{\Omega} = \cup_{i=1}^4 \Omega_i$  representing the full mesh correctly, i.e., without a preferred direction.

Let  $u^{(s,h)} = (u_1^{(s,h)}, u_2^{(s,h)}) \in \mathcal{NC}^h$ ,  $u^{(f,h)} = (u_1^{(f,h)}, u_2^{(f,h)}) \in \mathcal{W}^h$  be expressed in  $\tilde{\Omega}$  in terms of

the (local) basis associated with the nodal points in Fig.(1b) as follows

$$u_k^{(s,h)} = \sum_{j=1}^{12} \mathbf{u}_{k,j}^{(s,h)} \phi_j(x_1, x_2), \quad k = 1, 2, \quad (29)$$

$$u_1^{(f,h)} = \sum_{j=1}^6 \mathbf{u}_{1,2j}^{(f,h)} \psi_{2j}(x_1), \quad (30)$$

$$u_2^{(f,h)} = \sum_{j=1}^6 \mathbf{u}_{2,2j-1}^{(f,h)} \psi_{2j-1}(x_2). \quad (31)$$

Now choose in the weak form (22) the following test functions in  $\mathcal{V}^h$ :

$$\begin{aligned} v^{(1)} &= (\phi_1, \phi_1, 0, \psi_1), & v^{(2)} &= (\phi_4, \phi_4, \psi_4, 0), \\ v^{(3)} &= (\phi_7, \phi_7, 0, \psi_7), & v^{(4)} &= (\phi_{10}, \phi_{10}, \psi_{10}, 0), \end{aligned} \quad (32)$$

which ends up with an homogeneous algebraic sytem of four equations in 36 unknowns (the coefficients in Eq. (29), (30) and (31)).

Next, a standing plane wave -a function of the form

$$(U_0^s, V_0^s, U_0^f, V_0^f) e^{i(q_1^{(h)} x_1 + q_2^{(h)} x_2)},$$

where  $q^h = (q_1^{(h)}, q_2^{(h)})$  is the (discrete) wave vector, is proposed as a solution to the obtained system of four equations. The coefficients in the expansions (29), (30) and (31) are evaluated accordingly. For example, if the origin of coordinates is located at the center of  $\tilde{\Omega}$ , the coefficients for node 4 would be

$$\mathbf{u}_{4,1}^{s,h} = U_0^s e^{i\frac{1}{2}q_2^{(h)}h}, \quad \mathbf{u}_{4,2}^{s,h} = V_0^s e^{i\frac{1}{2}q_2^{(h)}h}, \quad \mathbf{u}_{4,1}^{f,h} = U_0^f e^{i\frac{1}{2}q_2^{(h)}h}.$$

After a rather cumbersome algebra the homogenous linear system

$$\mathcal{D}U = 0, \quad (33)$$

in the unknowns  $U = (U_0^s, V_0^s, U_0^f, V_0^f)$  is obtained. It is from this system that the numerical dispersion relations are derived, as explained in the next section.

It must be noticed that the process of adding the partial contributions of the stencils is a weighted one, with the weights coming from a shift to a common origin (23). Another choice to build the 'super-stencil' that correctly represents the full mesh could have been, as suggested in (36), to assign different approximate amplitudes to the degrees of freedom multiplying the plane wave, according to the considered direction.

As a final remark it is noticed that all the rather cumbersome algebraic manipulations related to the solutions of (33) both for the zero viscosity and viscous cases in Sections 5.1 and 5.2 were performed using the software package Mathematica (37).

## 5.1 The zero viscosity case

If the fluid is assumed to have zero viscosity the wave vector is real and can be written in polar form as  $q^{(h)} = q_m^{(h)}(\cos(\theta_1), \sin(\theta_1))$ , where  $\theta_1$  is the incidence angle. Besides, the phase

velocity  $c = \omega/q_m^{(h)}$  is constant, having different values for each wave type. In this case, Eq. (33) yields the generalized eigenvalue problem

$$c^2/V_R^2 \mathcal{M}U = -\mathcal{N}U. \quad (34)$$

Here

$$\mathcal{M} = 4h^2(q_m^{(h)})^2 \begin{pmatrix} -(A_2(5+C_1) + A_1(5+C_2)) & 0 & -4A_2\gamma_1(2+C_1) & 0 \\ 0 & A_2(5+C_1) + A_1(5+C_2) & 0 & 4A_1\gamma_1(2+C_2) \\ -A_2\gamma_1(5+6A_1A_2+C_1) & 0 & -4A_2\gamma_2(2+C_1) & 0 \\ 0 & -A_1\gamma_1(5+6A_1A_2+C_2) & 0 & -4A_1\gamma_2(2+C_2), \end{pmatrix} \quad (35)$$

and

$$\mathcal{N} = 96 \begin{pmatrix} A_2 - \delta_1(-A_1 + A_2C_1 + A_1C_2) & 2B_1B_2(A_2 + \delta_1(A_1 - 2A_2)) & -A_2\delta_2(C_1 - 1) & B_1d_2\delta_2 \\ 2B_1B_2(\delta_1(A_1 - 2A_2) - A_1) & -A_1 + \delta_1(-A_2 + A_2C_1 + A_1C_2) & -B_2D_1\delta_2 & A_1\delta_2(C_2 - 1) \\ -A_2\delta_2(C_1 - 1) & B_1D_2\delta_2 & -A_2\delta_3(C_1 - 1) & B_1D_2\delta_3 \\ B_2D_1\delta_2 & -A_1\delta_2(C_2 - 1) & B_2D_1\delta_3 & -A_1\delta_3(C_2 - 1). \end{pmatrix} \quad (36)$$

In the above matrices,

$$\begin{aligned} A_1 &= \cos\left(\frac{1}{2}hq_m^{(h)} \cos(\theta_1)\right), & A_2 &= \cos\left(\frac{1}{2}hq_m^{(h)} \sin(\theta_1)\right), \\ B_1 &= \sin\left(\frac{1}{2}hq_m^{(h)} \cos(\theta_1)\right), & B_2 &= \sin\left(\frac{1}{2}hq_m^{(h)} \sin(\theta_1)\right), \\ C_1 &= \cos(hq_m^{(h)} \cos(\theta_1)), & C_2 &= \cos(hq_m^{(h)} \sin(\theta_1)), \\ D_1 &= \sin(hq_m^{(h)} \cos(\theta_1)), & D_2 &= \sin(hq_m^{(h)} \sin(\theta_1)). \end{aligned} \quad (37)$$

Note that if  $\lambda$  denotes the wavelength,  $q_m^{(h)} = \frac{2\pi}{\lambda}$  and  $N_p = \frac{\lambda}{h}$  is the number of grid points per wavelength (recall that an homogeneous grid is being considered). Then  $hq_m^{(h)} = \frac{2\pi}{N_p}$ ; by replacing this expression in the two matrices written above, and setting  $P = \{\delta_1, \delta_2, \delta_3, \gamma_1, \gamma_2\}$ , the system (34) depends on  $P$ , the angle  $\theta$  between the wave vector and the  $x_1$ -axis and  $N_p$ , the number of points per wavelength.

Let  $\Lambda_i = \Lambda_i(P, \theta, N_p)$ ,  $i = I, II, S$  be the generalized eigenvalues of the system (34) associated with the compressional fast, slow and shear waves, respectively. Finally, the equation

$$v_{d,i} = \frac{\sqrt{\Lambda_i}}{\tilde{c}}, \quad i = I, II, S, \quad (38)$$

defines the dimensionless phase velocity, where for each  $\Lambda_i$ ,  $\tilde{c}$  is the correspondig analytic phase velocity as defined in equations (27) and (28) with  $\gamma_3 = 0$ .

For any fixed set of parameters  $P$  this dimensionless phase velocity yields the numerical dispersion properties of the algorithm; this is exemplified in Section 6.

## 5.2 The non-zero viscosity case

In this situation the wave vector  $q^{(h)}$  is complex, as in Eq (8) for the continuous case. Note that  $q^{(h)}$  can be written as

$$q^{(h)} = q^{(r,h)} - iq^{(i,h)} = q_m^{(r,h)}(\cos(\theta_1), \sin(\theta_1)) - iq_m^{(i,h)}(\cos(\theta_1 + \theta_2^h), \sin(\theta_1 + \theta_2^h)), \quad (39)$$

where  $\theta_2^h$  is the angle between the vectors  $q^{(r,h)}$  and  $q^{(i,h)}$ .

Proceeding as before, take the four test functions in (32) in the weak form (22) to get another algebraic linear system of four equations in 36 unknowns. By proposing plane wave solutions to this new linear system another homogeneous  $4 \times 4$  linear system

$$\tilde{\mathcal{D}}(\tilde{P}, \theta_1, \theta_2^h, N_p, h, q_m^{r,h}, q_m^{i,h})U = 0, \quad (40)$$

is obtained. The coefficients of the matrix  $\tilde{\mathcal{D}}$  are much more involved than the ones of the zero viscosity case; they also depend on expressions of the form  $\cos(\beta/2)$  and  $\cos(\beta)$ , where  $\beta = ihq_m^{(i,h)} \cos(\theta_1 + \theta_2^h)$  and similar ones replacing the cosines by sines one at a time and both simultaneously. Moreover, the system (40) cannot be written as a generalized eigenvalue problem, so in order to proceed the following steps are adopted: Let  $\tilde{P} = P \cup \{\gamma_3, \omega_a\}$  and set  $\theta_2^h = \theta_2$  in  $q^h$ , recalling that  $\theta_2$  is the angle between the vectors  $q^{(r)}$  and  $q^{(i)}$ . Fix  $N_p, \theta_1$  plus all parameters in  $\tilde{P}$ , and take  $h = 2\pi/(N_p q_m^r)$ . Asking for nontrivial solutions of (40) is equivalent to the validity of the following two conditions:

$$\begin{cases} \operatorname{Re} \left( \det(\tilde{\mathcal{D}}(\tilde{P}, \theta_1, \theta_2, N_p, h, q_m^{r,h}, q_m^{i,h})) \right) = 0, \\ \operatorname{Im} \left( \det(\tilde{\mathcal{D}}(\tilde{P}, \theta_1, \theta_2, N_p, h, q_m^{r,h}, q_m^{i,h})) \right) = 0. \end{cases} \quad (41)$$

Now (41) are two coupled nonlinear equations depending on just the two unknowns  $q_m^{r,h}$  and  $q_m^{i,h}$ .

The nonlinear system (41) was solved for a finite number of dimensionless frequencies  $\omega_a$  in the interval  $(0, \omega_t/\omega_c)$  using an iterative method, choosing as initial guesses the analytic  $q_m^r$ 's and  $q_m^i$ 's for each wave type.

## 6 NUMERICAL RESULTS

The analysis presented in the previous Sections was applied to study the dispersive properties of the finite element procedure (22) when the Biot medium is a sample of gas saturated Berea sandstone described in (38) as follows. The solid matrix has porosity  $\phi = .19$ , permeability  $k = 200$  millidarcies, and (dry) compressional and shear wave speeds of 3670 m/s and 2170 m/s, respectively. This yields values of  $K_m = 15.43$  GPa and  $\mu = 10.11$  GPa for the dry bulk and shear modulus. The grain material composing the solid matrix has density  $\rho_s = 2.65$  gr/cm<sup>3</sup> and bulk modulus  $K_s = 37.9$  GPa. The gas has viscosity  $\eta = 0.022$  centipoise, density  $\rho_f = 1.0$  gr/cm<sup>3</sup> and sound velocity 629.7 m/s, so that  $K_f = 0.05543$  GPa.

The corresponding dimensionless model parameters are:

$$\begin{aligned} \delta_1 &= 0.35, & \delta_2 &= 0.6 \cdot 10^{-2}, & \delta_3 &= .01, \\ \gamma_1 &= 0.06, & \gamma_2 &= 1.05, & \gamma_3 &= 0.12 \cdot 10^{-2}. \end{aligned}$$

The associated characteristic frequency is  $\omega_c = 6.59 \cdot 10^5$  Hz, and the critical frequency -recall that this is the frequency at which  $\gamma_2$  and  $\gamma_3$  become frequency dependent- is  $\omega_t = 7.6 \cdot 10^3$  Hz,

therefore, the considered frequency range is  $0 < \omega_a \leq 0.011$ .

Consider now the zero viscosity case, where in the continuous case phase velocities are frequency independent and the system is conservative (attenuation vanishes).

Figure 2 displays the behaviour of the dimensionless phase velocities  $v_d$  in (38) for the three wave types, in terms of the reciprocal of the number of points per wavelength and for different angles  $\theta_1$  in the range  $[0, \frac{\pi}{4}]$ . No more propagation directions are shown, because it turns out that the eigenvalues are invariant upon reflexions of the wave vector with respect to the  $x_1$ - and  $x_2$ - axes and the straight line  $x_2 = x_1$ .

It can be clearly seen that the slow wave is the most affected by numerical dispersion, with about 2% departure -for the worst propagation directions- between numerical and continuous phase velocities at ten points per wavelength.

In the next figures the more realistic viscous case, i.e.,  $\eta \neq 0$  is analyzed. In Figure 3 the dimensionless phase velocities for the three wave types are shown, as a function of the dimensionless frequency for different number of points per wavelength at a fixed direction. It can be seen that both the fast and shear waves display a negligible frequency dependent behavior; contrary to what happens with the slow wave. For the former waves the departure from the exact value is insignificant when using 20 points per wavelength, reaches about .5 % with 10 points per wavelength and climbs up to 2.5 % with 4 points per wavelength. The slow wave behavior is worse than that of the others; it shows a departure from the exact value of almost 2 % for some frequencies even using 10 points per wavelength, and the difference climbs up to 8 % when using 4 points per wavelength.

In Figure 4 the dimensionless group velocities  $\mathbf{v}_d^g$  for the three wave types under the same conditions as in Figure 3 are displayed. The same general behavior that was just described is reproduced here with all curves lifted upwards (in the sense that they are farther from the exact value). Notice that in all displayed cases the group velocity was numerically calculated from the computed values of the corresponding phase velocity, since as explained before the discrete wave vector  $q^{(h)}$  is obtained from (41) only for a finite number of frequencies.

In Figure 5 the dimensionless attenuation coefficient  $\xi_{d,l} = q_{m,l}^{(i,h)} / q_{m,l}^{(i)}$ ,  $l = I, II, S$  is displayed; all three waves show the same dependence with frequency as in Figure 3, but they worsen their numerical dispersive behavior; this is more evident for the shear wave, where with  $N_p = 20$  the error is slightly more than 1 % and for  $N_p = 10$  the error is almost 5%.

Figure 6 displays the results in a different fashion. Here the dimensionless phase velocities for the three waves are displayed as function of the reciprocal of the number of points per wavelength for a given fixed frequency. In this way, it can be analyzed how the waves behave when changing the propagation direction. The three waves present the same symmetries as in the non-viscous case, therefore it is only necessary to depict angles  $\theta_1$  lying in the interval  $[0, \frac{\pi}{4}]$ ; from there four representative cases were chosen. As expected, the fast and shear waves are less affected by numerical anisotropy than the slow wave; however, there is a noticeable dependence of the three numerical waves with the propagation direction. Some directions are better behaved than others; nevertheless, in order to establish a bound, the worst case must be considered. Then, taking for example  $N_p=5$ , the fast and shear waves have an error of about 1.5%, while the slow wave has an error of almost 9% for  $\theta_1 = \frac{\pi}{4}$ . All directions, as expected, converge to the exact solution when increasing the number of points per wavelength, but although the fast and shear waves do it fairly fast -with  $N_p=10$  they lie well within the 1% error bound- it is necessary to use almost twice the number of points for all propagation directions for the slow wave to behave likewise. Accordingly to this situation, for small  $N_p$ 's the slow wave display big errors, that is why the abscissae range for this wave in the figure was reduced; it is not meaningful to use less

than four points per wavelength if the error is about 14% for this discretization level.

Finally, Figure 7 shows the dimensionless attenuation coefficients  $\xi_d$  for the three waves as a function of  $N_p$  for different propagation directions at a fixed frequency. Although for the slow and shear waves there is a direction for which almost no quality loss is observed even with small number of points per wavelength, the general behavior is dependent on the propagation direction. Notice that the distance between numerical and exact solution strongly increased when  $N_p$  is diminished. For example, all the considered directions of the fast wave lie within a 1% error bound for  $N_p = 20$ , but they reach a 3% when the number of points is halved; the situation is worse for the other two waves, with 20 points per wavelength they also are within a 1% error bound (but closer to it than the fast wave) and reaching a 4% relative error for  $N_p = 10$  and even a 9% error for  $N_p = 6$ .

As a final remark, it should be recalled that in the performed analysis the element size  $h$  is different for each wave because it is calculated, as previously explained, as  $h = 2\pi/(N_p q_{m,i}^r)$ ,  $i = I, II, S$ . In practice the grid size will be fixed so as to obtain a  $N_p$  that guarantees a certain error bound for the worst behaved wave, i.e., the slow wave. This is the wave with shortest wavelength (greatest wave vector modulus), and automatically the shear and fast waves will fall, as already observed, within the same error bound. In fact, they will be “overestimated”, leading to an unavoidable increase of the computation time, unless certain loss in accuracy in the calculation of the slow wave is accepted.

The results here obtained are of importance for example when performing numerical experiments to simulate wave propagation in heterogeneous saturated poroelastic materials modeling mesoscopic loss mechanisms due to wave induced fluid flow (39). In this particular application, a very accurate calculation of the slow mode is critical in order to properly compute the physical attenuation.

## 7 CONCLUSIONS

An analysis of the numerical dispersion properties of a finite element method used to approximate wave propagation in a Biot medium has been presented. The used finite element method comprises a nonconforming rectangular element for the approximation of each component of the displacement vector in the solid phase, and the Raviart-Thomas-Nedelec mixed finite element space of zero order ( $RTN_0$ ) -which is a conforming space- for the fluid phase.

The study was performed by constructing and analyzing analytic and numerical dimensionless dispersion relations, and by evaluating derived quantities such as dimensionless phase and group velocities and dimensionless attenuation for the three type of waves predicted by Biot. Further, two cases were separately considered; the first one where no viscosity is present, leading to frequency independent numerical dispersion relations with no attenuation, and the more realistic viscous case, leading to dispersion relations involving frequency dependent attenuating waves. In the last case the low-frequency range was considered, so that the mass and viscous coupling coefficients are frequency independent.

It was observed that the analyzed numerical method introduces both numerical dispersion and anisotropy; being the loss of accuracy in the numerical solution more severe for the slow wave than for the fast or shear waves in most of the analyzed cases.

As the performed analysis is local in the sense that the results are shown in terms of the number of points per wavelength, it should be expected that when performing a simulation of wave propagation in a Biot medium, if the computational domain comprises several wavelengths, the dispersion error will be incremented accordingly. The fact that the attenuation behaves worse for all three waves than the group velocity, would suggest to decrease the number of points

per wavelength if the interest is in computing arrival times, and not in amplitudes. Finally, as a rule of thumb derived from the presented analysis, it is concluded that using 10 points per wavelength of the slow wave the error in the group velocities and attenuation coefficients for the three waves is smaller than 2 %, and 4%, respectively.

## Acknowledgments

This work was partially supported through grants PICT 03-13376 (ANPCyT) and PIP 04-5126 (CONICET)

## REFERENCES

- [1] M. A. Biot. Theory of propagation of elastic waves in a fluid-saturated porous solid. I. Low frequency range. *J. Acoust. Soc. Amer.*, 28:168–171, 1956.
- [2] M. A. Biot. Theory of propagation of elastic waves in a fluid-saturated porous solid. II. High frequency range. *J. Acoust. Soc. Amer.*, 28:179–191, 1956.
- [3] M. A. Biot. Mechanics of deformation and acoustic propagation in porous media. *J. Appl. Phys.*, 33:1482–1498, 1962.
- [4] J. E. Santos and D. Sheen. Finite element methods for the simulation of waves in composite saturated poroviscoelastic media. *Siam J. Numer. Anal.*, to appear, 2006.
- [5] J. Douglas, Jr., J. E. Santos, D. Sheen, and Ye. X. Nonconforming Galerkin methods based on quadrilateral elements for second order elliptic problems. *RAIRO Mathematical Modelling and Numerical Analysis (M2AN)*, 33:747–770, 1999.
- [6] P. A. Raviart and J. M. Thomas. Mixed finite element method for  $2^{nd}$  order elliptic problems. *Mathematical Aspects of the Finite Element Methods, Lecture Notes of Mathematics, vol. 606, Springer, 1975.*
- [7] J. C. Nedelec. Mixed finite elements in  $\mathbf{R}^3$ . *Numer. Math.*, 35:315–341, 1980.
- [8] A. Bayliss, C. Goldstein, and E. Turkel. On accuracy conditions for the numerical computation of waves. *J. Comp. Phys.*, 59:396–404, 1985.
- [9] F. Ihleburg and I. Babuska. Dispersion analysis and error estimation of Galerkin finite element methods for the Helmholtz equation. *Intl. J. for Numerical Methods in Engineering*, 38:3745–3774, 1995.
- [10] F. Ihleburg and I. Babuska. Finite element solution of the helmholtz equation with high wave number Part I: the  $h$ -version of the FEM. *Computers Math. Applic.*, 30(9):9–37, 1995.
- [11] F. Ihleburg and I. Babuska. Finite element solution of the helmholtz equation with high wave number Part II: the  $h-p$ -version of the FEM. *SIAM J. Numer. Anal.*, 34(1):325–358, 1997.
- [12] F. Ihleburg and I. Babuska. Reliability of finite element methods for the numerical computation of waves. *Advances in Engineering Software*, 28(7):417–424, 1997.
- [13] A. Bamberger, G. Chavent, and P. Lailly. Etude de schémas numériques pour les équations de l'élastodynamique linéaire. Technical Report 41, INRIA, 1980.
- [14] K.J. Marfurt. Accuracy of finite-difference and finite-element modelling of the scalar and elastic wave equations. *Geophysics*, 49:533, 1984.
- [15] F. I. Zyserman, P. M. Gauzellino, and J. E. Santos. Dispersion analysis of a nonconforming finite element method for the Helmholtz and elastodynamic equations. *Int. J. Numer. Meth. Engng.*, 58:1381–1395, 2003.
- [16] F. Zyserman and P. Gauzellino. Dispersion analysis of a nonconforming finite element

- method for the three dimensional scalar and elastic wave equations. *Finite elements in analysis and design*, 41:1309–1326, 2005.
- [17] L. L. Thompson and P. M. Pinsky. A Galerkin least squares finite element method for the two dimensional Helmholtz equation. *Int. J. Numer. Methods Eng.*, 38(3):371–397, 1995.
- [18] I. Babuska, S. Sauter, and E. Paik. A generalized finite element method for solving the Helmholtz equation in two dimensions with minimal pollution. *Computer Methods in Applied Mechanics and Engineering*, 128:325–359, 1995.
- [19] C. Jo, C. Shin, and J. Suh. An optimal 9-point finite-difference, frequency-space, 2-D scalar wave extrapolator. *Geophysics*, 61:529–537, 1996.
- [20] O. Cessenat and B. Despres. Application of an ultra weak variational formulation of elliptic PDEs to the two-dimensional Helmholtz problem. *SIAM J. Numer. Anal.*, 35:255–299, 1998.
- [21] J.L. Cipolla. Subgrid modeling in a Galerkin method for the Helmholtz equation. *Comput. Methods Appl. Mech. Engrg.*, 177:35–49, 1999.
- [22] A. Oberai and P. Pinsky. A residual-based finite element method for the Helmholtz equation. *Int. J. Num. Meth. Engineering*, 49:399–419, 2000.
- [23] C. Farhat, I. Harari, and U. Hetmaniuk. A discontinuous Galerkin method with Lagrange multipliers for the solution of Helmholtz problems in the mid-frequency regime. *Comput. Methods Appl. Mech. Engrg.*, 192:1389–1419, 2003.
- [24] G. B. Alvarez, A. F. D. Loula, E. G. Dutra do Carmo, and F. A. Rochinia. A discontinuous finite element formulation for the Helmholtz equation. *Comput. Methods Appl. Mech. Engrg.*, 195(33-36):4018–4035, 2006.
- [25] A. F. D. Loula, G. B. Alvarez, E. G. Dutra do Carmo, and F. A. Rochinia. A discontinuous finite element method at element level for the Helmholtz equation. *Comput. Methods Appl. Mech. Engrg.*, 2006. available online at [www.sciencedirect.com](http://www.sciencedirect.com), corrected proof.
- [26] J. E. Santos, J. M. Corberó, C. L. Ravazzoli, and J. L. Hensley. Reflection and transmission coefficients in fluid-saturated porous media. *J. Acoust. Soc. Amer.*, 91:1911–1923, 1992.
- [27] F. Gassmann. Über die elastizität poröser medien (On the elasticity of porous media). *Vierteljahrsschrift der Naturforschenden Gessellschaft in Zurich*, 96:1–23, 1951. CHE 1856-1999 246.
- [28] D. L. Johnston, J. Koplik, and R. Dashen. Theory of dynamic permeability and tortuosity in fluid-saturated porous media. *J. Fluid Mechanics*, 176:379–402, 1987.
- [29] J. M. Carcione. Wave fields in real media: Wave propagation in anisotropic, anelastic and porous media. *Handbook of Geophysical Exploration, Pergamon Press Inc.*, 31, 2001.
- [30] N. C. Dutta and H. Odé. Seismic reflection from a gas water contact. *Geophysics*, 48:148–162, 1983.
- [31] C. W. Holland and B. A. Brunson. The Biot-Stoll sediment model: An experimental assesment. *J. Acoust. Soc. Amer.*, 84:1437–1443, 1988.
- [32] J. M. Hovem and G. D. Ingram. Viscous attenuation of sound in saturated sand. *J. Acoust. Soc. Amer.*, 66:1807–1812, 1979.
- [33] J. Bear. Dynamics of fluids in porous media. *Dover Publications, New York*, 1972.
- [34] J. E. Santos, J. Douglas, Jr., M. E. Morley, and O. M. Lovera. Finite element methods for full waveform acoustic logging. *IMA Journal of Numerical Analysis*, 8:415–433, 1988.
- [35] G. Cohen. *Higher-order numerical methods for transient wave equations*. Springer, 2002.
- [36] I. Babuska, T. Stroboulis, C. Upadhyay, S. Gangaraj, and K. Copps. Validation of a posteriori error estimation by a numerical approach. *International Journal for Numerical Methods in Engineering*, 37:1073, 1994.

- [37] Inc. Wolfram Research. *Mathematica, Version 5.2*. Wolfram Research, Inc., 2005.
- [38] J. H. Rosenbaum. Synthetic microseismograms: logging in porous formations. *Geophysics*, 39:14–32, 1974.
- [39] J. M. Carcione and S. Picotti. P-wave seismic attenuation by slow-wave diffusion: effects of inhomogeneous rocks properties. *Geophysics*, 71:01–08, 2006.

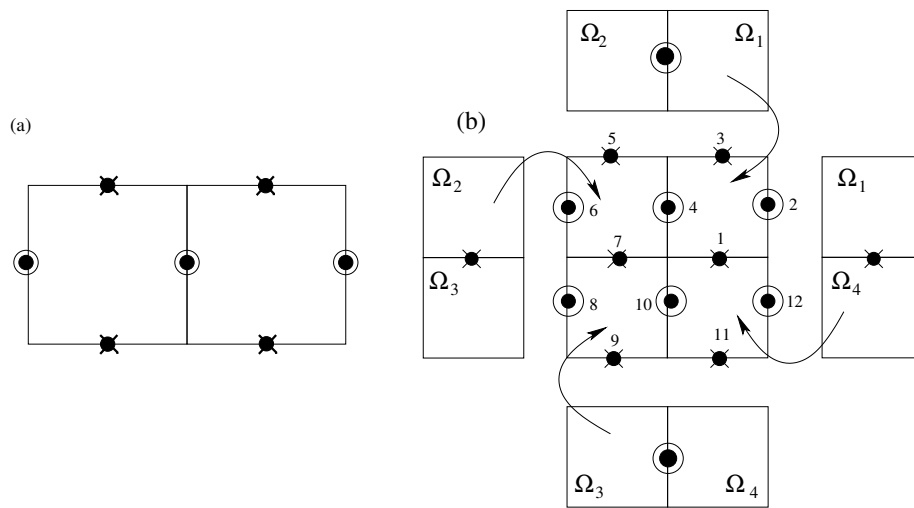


Figure 1: The figure on the left shows the degrees of freedom of a NC-stencil. However, in order to perform a dispersion analysis of the NCFEM method, a stencil without preferred directions is needed. The figure on the right shows a scheme of how it is obtained. In both figures the filled circles represent the degrees of freedom corresponding to the solid, the circle to the  $x_1$ -component of the fluid and crosses to the  $x_2$ -component of the fluid.

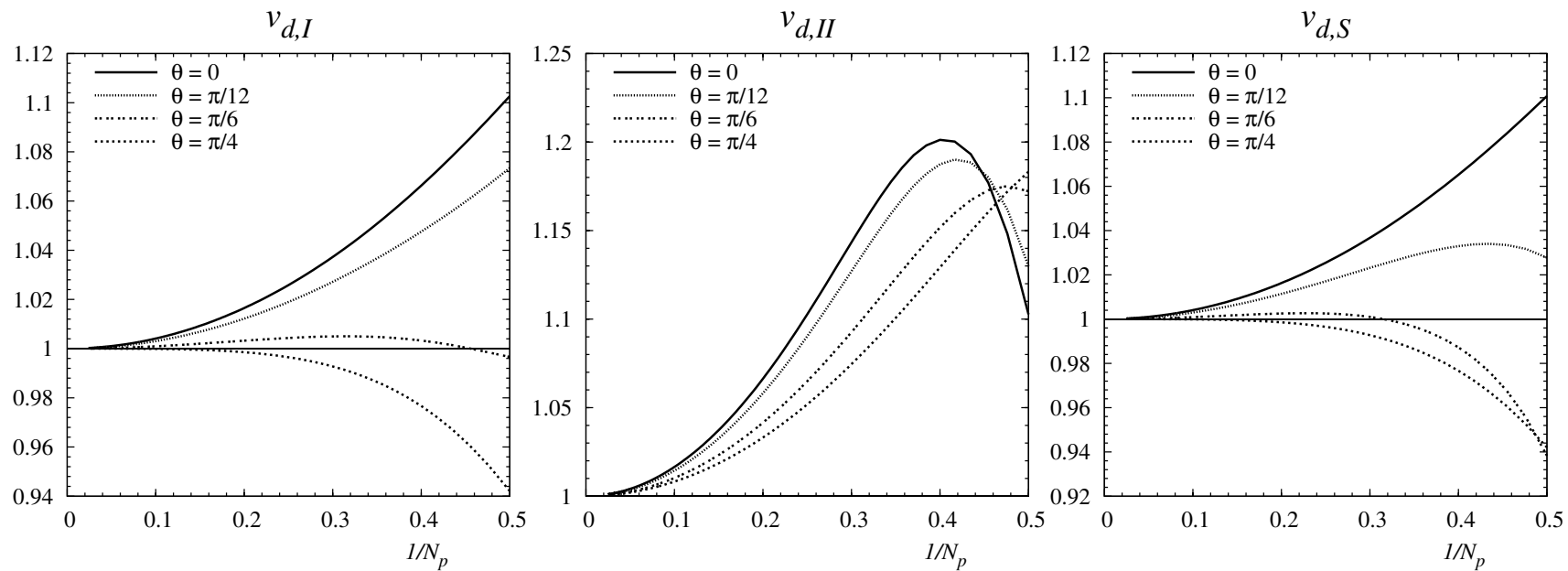


Figure 2: Non-viscous case. Dimensionless phase velocities for the fast (left), slow (middle) and shear waves (right) as a function of the reciprocal of the number of points per wavelength for different propagation directions.

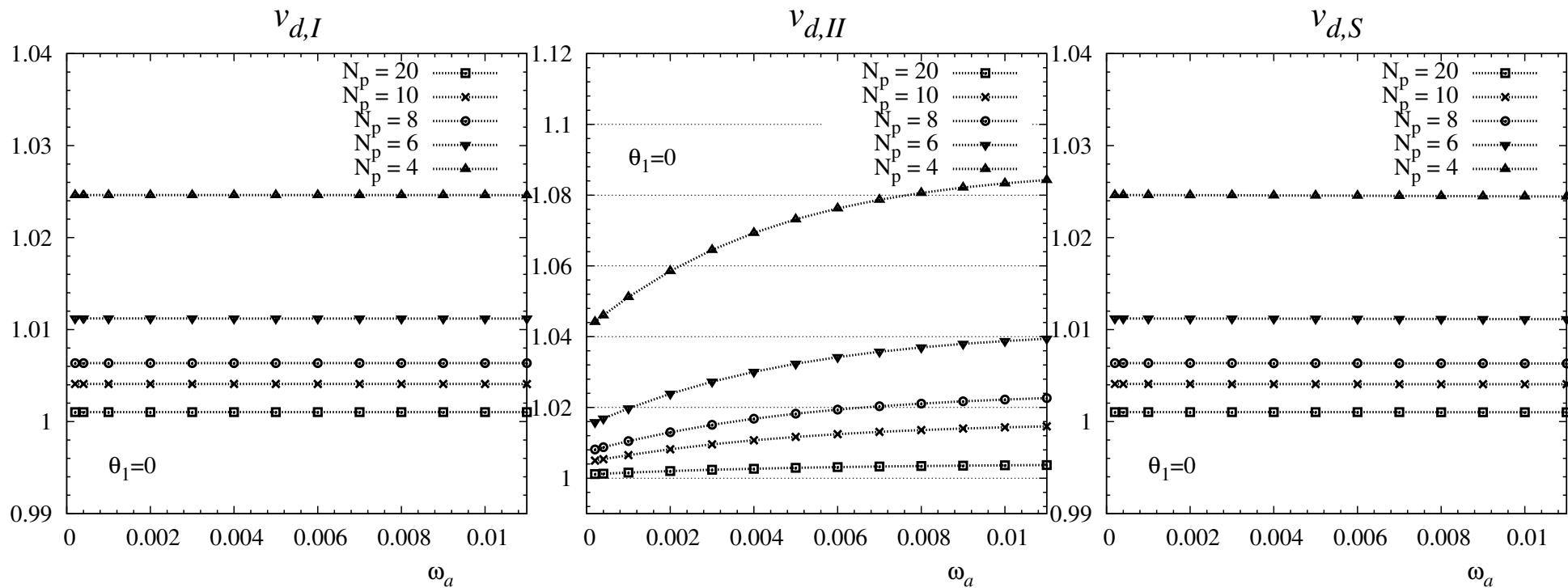


Figure 3: Viscous case. Dimensionless phase velocities for the fast (left), slow (middle) and shear waves (right), as a function of the frequency, for different numbers of points per wavelength. Only one propagating direction is depicted; for most cases this corresponds to the worst one.

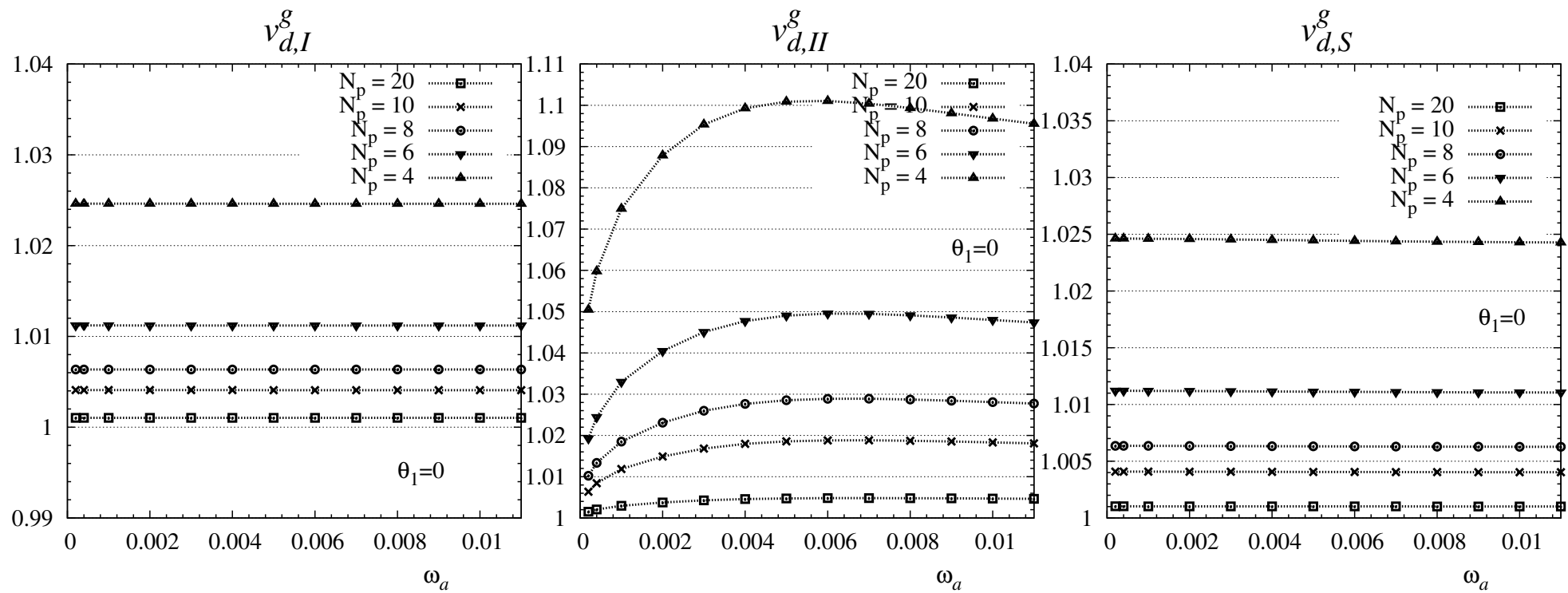


Figure 4: Same as Fig.3 for the group velocity case.

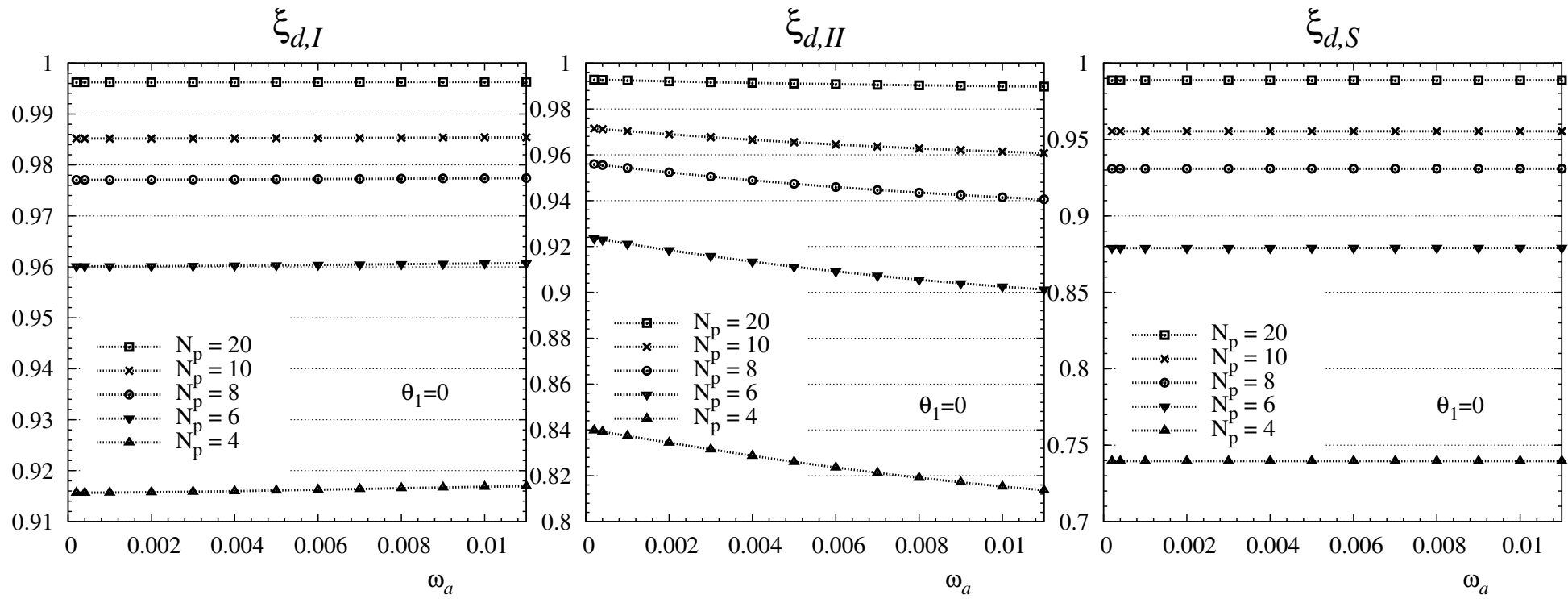


Figure 5: Same as Fig.3 for the attenuation.

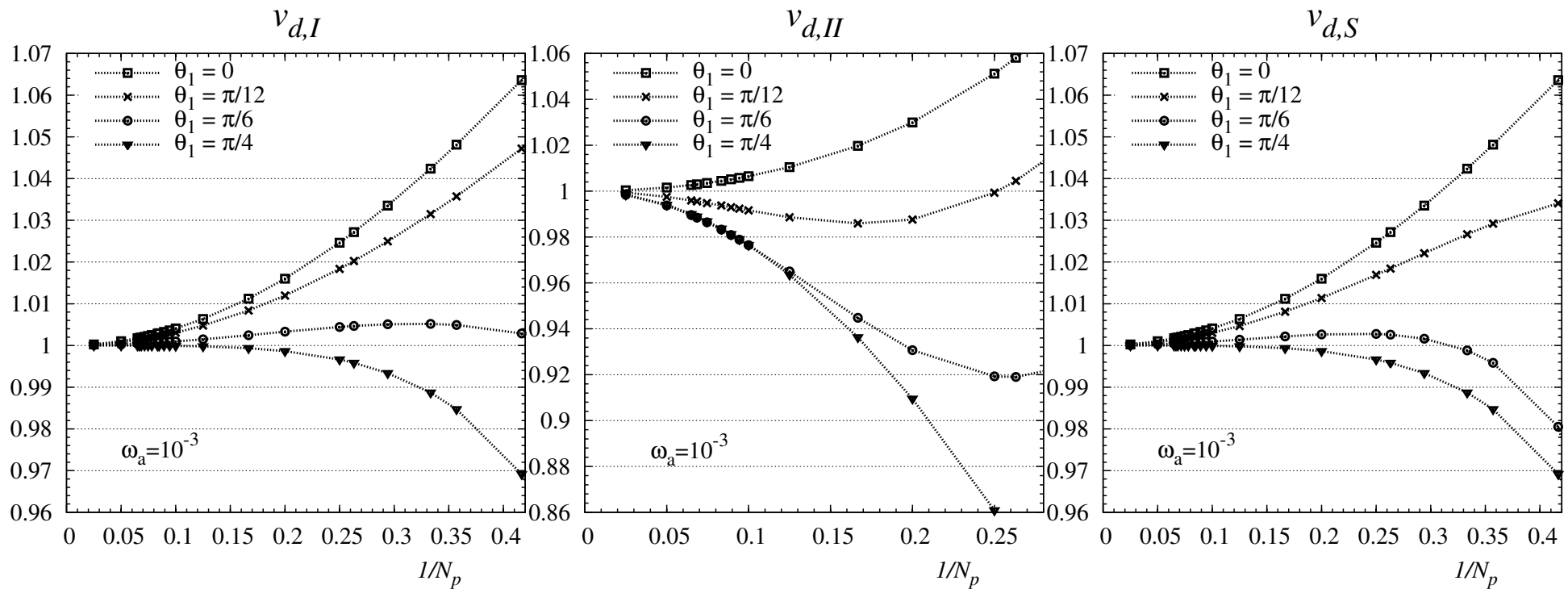


Figure 6: Viscous case. Dimensionless phase velocities for the fast (left), slow (middle) and shear (right) waves, as a function of the reciprocal of the number of points per wavelength at a fixed frequency for different propagation directions.

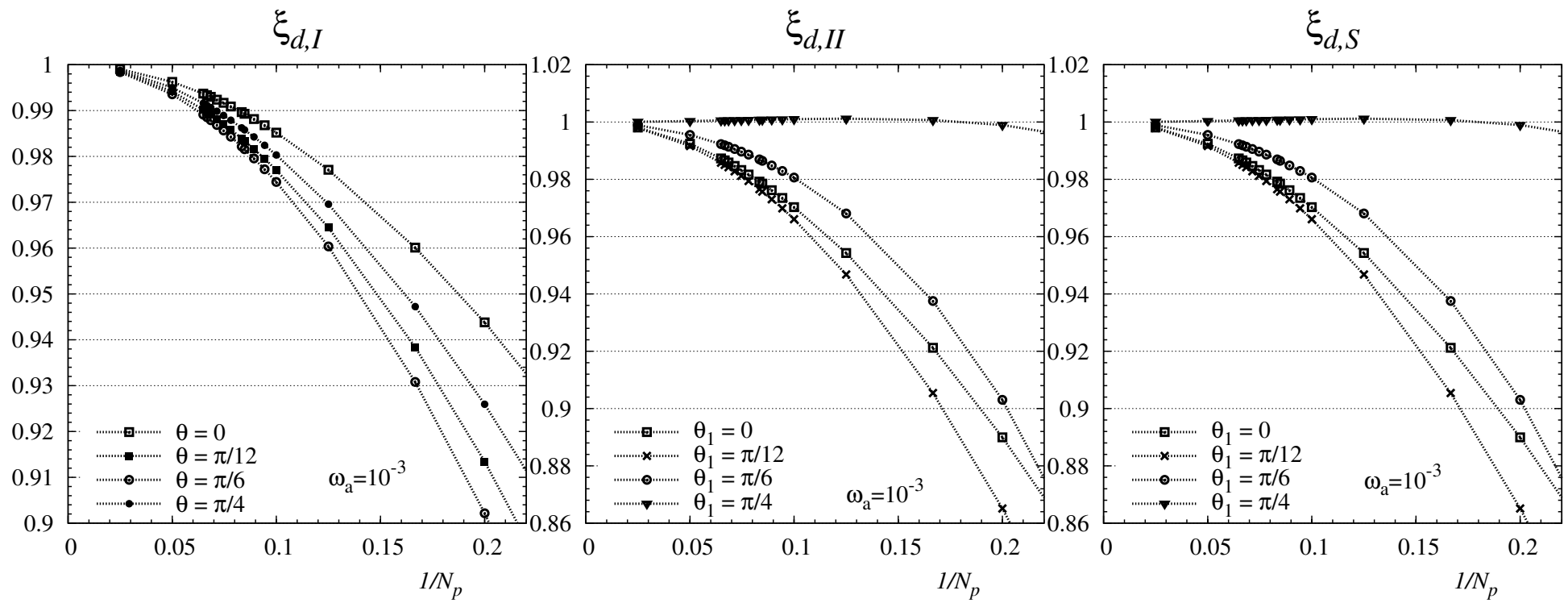


Figure 7: Viscous case. Dimensionless attenuations for the fast (left), slow (middle) and shear (right) waves, as a function of the reciprocal of the number of points per wavelength at a fixed frequency for different propagation directions.